1

Imaging Magnetic Microspectroscopy

W. Kuch

There are several well established techniques for spectroscopy of magnetic films and surfaces that are commonly employed when information about electronic states, binding properties, or element-resolved magnetic properties is required. The reduction in lateral size that goes along with the soaring extent to which magnetic elements and devices are used or planned to be used in technological applications in magnetic sensors, data storage, or magneto-electronics demands magnetic spectroscopic information on a microscopic lateral length scale. Thus, the combination of magnetic spectroscopy and microscopy into what is commonly termed microspectroscopy or spectromicroscopy would be ideal for the study of small magnetic structures.

This chapter explains the combination of photoelectron emission microscopy (PEEM) and X-ray magnetic circular dichroism (XMCD) in absorption for imaging XMCD-PEEM microspectroscopy. In a PEEM, an electrostatic electron optics creates a magnified image of the secondary electron intensity distribution at the sample surface. When excited by soft X-rays, the image intensity can thus be regarded as a local electron yield probe of X-ray absorption. In XMCD, the measurement of the total electron yield of the sample is frequently used to determine the X-ray absorption as a function of photon energy and helicity of the circularly polarized radiation. Consequently, scanning the photon energy and recording PEEM images at each photon energy step for both helicities results in a microspectroscopic data set that allows one to extract the full information that is usually obtained from XMCD spectra for each single pixel of the images. Of particular interest is therefore the application of the so-called sum rules to extract the effective spin moment and the orbital moment, projected onto the direction of incoming light. This chapter starts with a short overview of magnetic microspectroscopy techniques in comparison to XMCD-PEEM microspectroscopy. The basics of the underlying spectroscopic and microscopic methods are briefly explained in Sect. 1.2. Important experimental aspects inherent to XMCD-PEEM microspectroscopy are discussed in Sect. 1.3. Finally, in Sect. 1.4, two recent examples of application of XMCD-PEEM microspectroscopy are presented, in which the method has proven beneficial for the study of interesting issues in the field of ultrathin magnetic films.

1.1 Microspectroscopy and Spectromicroscopy – An Overview

The terms "microspectroscopy" and "spectromicroscopy" both refer to techniques that combine spectroscopy and microscopy. "Spectromicroscopy" is commonly used to describe microscopic imaging techniques in which the image contrast is due to spectroscopic details. The acquired images are then related to a certain energy of either electrons or photons. "Microspectroscopy," on the other hand, is primarily used to describe techniques in which spectroscopic information is obtained from a small area on a sample. In terms of the dependence of information gained, spectromicroscopy is thus a technique that yields data as a function of the two space coordinates for a certain value of the energy coordinate, whereas microspectroscopy delivers data as a function of energy for a fixed pair of values of the space coordinates. The consequent extension of both spectromicroscopy and microspectroscopy would be to get the full spectroscopic *and* spatial information in the same measurement. That is, data are obtained as a function of all three variables, namely, the two space coordinates and energy. In that limit, "spectromicroscopy" and "microspectroscopy" become identical. The topic of this contribution is the combination of X-ray magnetic circular dichroism (XMCD) and photoelectron emission microscopy (PEEM) for the measurement of such a three-dimensional data set. It may be considered as either full-image microspectroscopy or full-energy spectromicroscopy, where we (arbitrarily) have chosen the former name, and thus will refer to it as "microspectroscopy". In all cases, the extension to full-image microspectroscopy, or imaging microspectroscopy, represents a considerably higher experimental effort, and it will be only practical if the gain in information makes it worthwhile.

In this section, a short overview of some microspectroscopic and spectromicroscopic techniques used for the investigation of magnetic samples is given, and the use of XMCD-PEEM as an ideal imaging microspectroscopic technique is motivated. A more comprehensive overview of spectromicroscopic techniques for non-magnetic applications can be found in [1].

1.1.1 Scanning Techniques

In microscopy, one can generally distinguish between scanning techniques and techniques that use parallel imaging. We will start with the scanning techniques. A scanning technique that is commonly employed at most synchrotron light sources and can be used for magnetic microspectroscopy is scanning X-ray microscopy (SXM). The incident X-ray radiation from the synchrotron is focused with appropriate X-ray optics, for example, by Fresnel zone plates, into a small spot on the sample. Depending on the photon energy range, spot sizes smaller than 200 nm have been achieved [2, 3]. In plain microscopy applications, the sample is scanned and the transmitted X-rays generate the microscopic image. With only minor modifications such setups can easily be used for spectromicroscopy or microspectroscopy. For magnetic microspectroscopy in the simplest case, the dependence of the transmitted, absorbed, or reflected X-ray intensity on photon energy is recorded. Magnetic contrast is obtained from the dependence on magnetization direction of the X-ray absorption cross section at elemental absorption edges when circular polarization is used (see Sect. 1.2.1). Another variant includes electron spectroscopy, where emitted electrons of a certain kinetic energy are detected [4]. Here, magnetic contrast can be obtained from magnetic dichroism in photoelectron spectroscopy, which is the difference in photoelectron intensity upon variation of magnetization direction or X-ray polarization [5]. Since the magnetic contrast is higher in absorption, only this has been used for magnetic imaging [6, 7]. The advantage of scanning X-ray microscopy is that the microscopy component of the technique is completely in the excitation path, so that on the detection path standard spectrometers can be used to provide the spectroscopy component. The energy resolution for electron detection can thus be chosen to be the same as in plain photoelectron or Auger electron spectroscopy. For imaging microspectroscopy, however, the disadvantage, as in all scanning techniques, is that the time needed for a complete scan of both the sample position and the energy can be quite long.

Another scanning spectromicroscopic technique for imaging magnetic properties is spin-polarized scanning tunneling microscopy, in which the spin-dependence in electron tunneling between ferromagnets is used as a contrast mechanism (see Chaps. 9,10). In one approach, the tip magnetization is periodically reversed (Chap. 9), while another approach relies on differential electron tunneling spectroscopy (Chap. 10). In the latter, the bias voltage between a magnetic tip and the sample is set to an energy at which the dependence of the tunnel current on the direction of sample magnetization is maximized [8,9]. Without changing the experimental setup microspectroscopy can also be performed. For this, the tip position is kept fixed and the bias voltage is varied. In principle imaging scanning tunneling microspectroscopy is also possible. Due to restrictions in acquisition times, however, in most cases this is used only to find the best energy for obtaining magnetic domain images.

For the imaging of magnetic domains, laser scanning Kerr microscopy has also been used [10]. The magneto-optical Kerr effect using visible light is a commonly employed method to measure magnetization curves. The spectroscopic variant, Kerr spectroscopy, where the wavelength of the exciting laser light is scanned, is used for the characterization of electronic properties [11]. No reports exist, however, of imaging scanning Kerr microspectroscopy measurements.

As mentioned before, in general, the disadvantage of all scanning techniques for imaging microspectroscopy is that three parameters, namely, two space coordinates *and* the energy, need to be scanned step by step, which can make it a rather lengthy undertaking. Consequently, in most cases, the relation between effort and benefit does not favor imaging scanning microspectroscopy.

1.1.2 Imaging Techniques

Parallel imaging techniques have the advantage over scanning techniques in that for imaging microspectroscopy only the energy needs to be scanned, while at each energy step a complete image is acquired. Parallel imaging techniques may, therefore, be accelerated to achieve feasible measuring times even for full image microspectroscopy. The individual images are equivalent to two-dimensional sets of data points, which are acquired in parallel. Parallel imaging of magnetic spectroscopic information is based either on magneto-optical effects or on magneto-dichroic effects in electron spectroscopy after optical excitation.

An example of magneto-optical effects [12] is the magneto-optical Kerr effect using visible light, as already mentioned in the previous section. In the microscopic variant, optical microscopy is used to convert the magneto-optical information into a domain image of the sample [10]. The gain in information that would result from the combination of Kerr microscopy with wavelength scanning Kerr spectroscopy, however, does not seem worth the effort, since no imaging Kerr microspectroscopy has been reported in literature up until now.

This differs in the range of soft X-rays, where elemental core level absorption edges are accessed. The optical constants vary strongly in the vicinity of these edges and depend on the magnetization of the sample. The absorption of circularly polarized X-rays at the absorption edges depends on the relative orientation between light helicity and magnetization direction. This mechanism, which will be presented in the following section, is named X-ray magnetic circular dichroism (XMCD) in absorption, and is the first choice for obtaining magnetic contrast in imaging. It has been demonstrated, though, that in principle magnetic circular dichroism in angle-resolved photoemission can also be used to obtain magnetic contrast in photoelectron spectromicroscopy. Images obtained in an imaging hemispherical electron analyzer from Fe $3p$ photoelectrons after off-resonant excitation with circular polarization exhibited a weak magnetic contrast [13]. In a more recent paper, magnetic contrast was claimed even using unpolarized light from an X-ray tube and magnetic dichroism in Fe $2p$ photoemission [14]. The signal-to noise ratio, however, is significantly worse in the photoemission case compared to images obtained in the same instrument using XMCD in absorption to generate magnetic contrast [15, 16].

Two ways can generally be used to image the local X-ray absorption: either by imaging photons, or by imaging emitted electrons. Imaging the transmitted photons has been successfully performed for magnetic spectromicroscopic domain imaging in a transmission X-ray microscope [17]. The sample is thereby prepared such that its total thickness allows the transmission of soft X-rays, and a zone plate–based X-ray optics is used to create the image of the transmitted beam. In general, the drawback for microspectroscopy with photon imaging techniques stems from problems due to the energy dependence of the focal length of X-ray optics, in particular, of zone plates. The magnification and focusing of the resulting image, therefore, varies during a photon energy scan, which leads to a significant blurring of the image if no correction, for example, by a sophisticated image processing software, is performed.

In that respect, the imaging of the distribution of emitted electron intensity for microspectroscopic purposes is clearly easier. Since just the X-ray absorption needs to be detected as a function of photon energy, no explicit energy filtering of the electrons is necessary and the high intensity secondary electrons may be used. X-ray optics, if any, are used only for the illumination of the imaged area of the sample. Different types of electron optics have been employed successfully for XMCD-based spectromicroscopic imaging of magnetic domains, all of which are classified under the name "electron emission microscopy". While in most of the more recent work fully

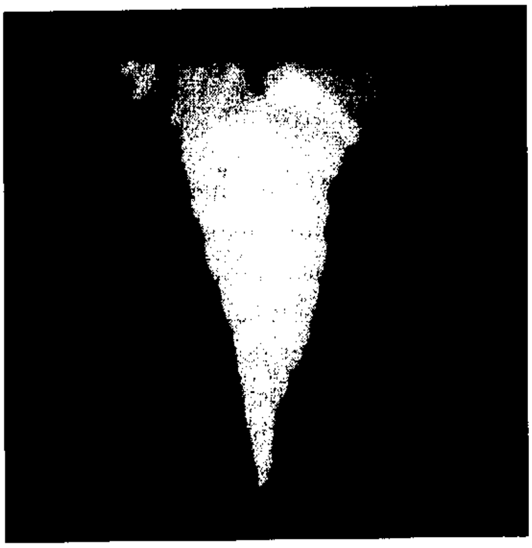

Fig. 1.1. Magnetic domain image of a triangular microstructure of 30-nm-thick polycrystalline Co on Si using a PEEM and XMCD. Field of view is $40 \times 40 \mu m^2$

electrostatic photoelectron emission microscopes (PEEMs) (see Sect. 1.2.2) were used [18–23], an imaging hemispherical electron analyzer [15, 16], and in [24] a low energy electron microscope (LEEM, [25, 26]) have also been employed. Note that the latter is different from magnetic imaging by spin-polarized LEEM, which is presented in Chap. 6. Figure 1.1 shows an example of a domain image taken with a PEEM. It shows a lithographic triangular microstructure of 30-nm-thick polycrystalline Co. Different grayscale contrast represents different directions of magnetization, where bright means pointing up, dark pointing down, and intermediate gray indicates a horizontal magnetization direction [27].

The advantage of extending XMCD-based spectromicroscopy with electron detection to imaging microspectroscopy is obvious: Experimentally, it is quite straightforward if some aspects, as outlined in Sect. 1.3, are considered. XMCD is a widely used and comparably well understood spectroscopic technique, so there is a significant gain in quantitative information from full-image microspectroscopy compared with the acquisition of spectromicroscopic images; this will be discussed in Sect. 1.2.1. Finally, due to the availability of high-brilliance insertion-device beamlines at third-generation synchrotron radiation light sources, the time required for recording three-dimensional data sets for imaging microspectroscopy is approaching feasibility while still maintaining reasonable spatial resolution. This will be demonstrated by selected examples in Sect. 1.4.

A further advantage of X-ray absorption–based spectromicroscopy is that by using linearly polarized X-rays, a magnetic-dichroic signal can also be obtained from oxidic antiferromagnets [28, 29]. The use of this X-ray linear magnetic dichroism for the imaging of antiferromagnetic domains is outlined in Chap. 2.

In the remainder of this chapter, PEEM is assumed as the electron emission microscopy technique for magnetic X-ray absorption spectroscopy. This is due to the existing work in this field, although, most of what is described is also valid for any other type of electron emission microscopy.

1.2 Basics

1.2.1 X-Ray Magnetic Circular Dichroism

Since its experimental discovery [30], magnetic circular dichroism in soft X-ray absorption has developed into a widely used technique for the element-specific characterization of magnetic films and multilayers. This is in part due to the so-called sum rules that have been proposed to deduce quantitative magnetic information from XMCD spectra [31, 32]. Other reasons for the widespread use of XMCD are: The magnetism-related changes in the absorption cross section are quite large; there are several synchrotron radiation light sources around the world providing X-rays of tunable wavelength, and it is comparatively easy to measure X-ray absorption from the total photoelectron yield, where only the sample current has to be detected.

This section is aimed at providing the reader who is not familiar with XMCD spectroscopy with the basic ideas in order to follow the remainder of the chapter. More comprehensive introductions can be found elsewhere [12, 22, 33–36].

We will restrict ourselves to the $L_{2,3}$ absorption edges of $3d$ transition metals, i.e., the onset of excitation of transitions of $2p$ core electrons to empty states above the Fermi level. Let us for the moment consider absorption in a paramagnet. An explanation of X-ray absorption spectroscopy in a one-electron description is shown in Fig. 1.2. The left upper panel shows a schematic representation of the occupied density of states of the $2p$ core levels. The important point here is that because of spin-orbit interaction, the $2p$ states are energetically split into the clearly separated $2p_{1/2}$ and $2p_{3/2}$ levels. Any further splitting into sublevels is not important here. Absorption of X-rays by the excitation of electronic transitions from the $2p$ states is determined by the occupied density of states of the $2p$ core electrons and the unoccupied density of states available for these transitions above the Fermi energy (E_F). The latter is schematically shown in the upper right panel, where the shaded area represents the unoccupied states. The contribution from states of predominantly s, p character is represented by flat energy dependence, whereas d states are shown as sharp peaks around E_F. The resulting absorption spectrum is obtained from the convolution of the occupied density of states of the left upper panel and the unoccupied density of states of the right upper panel. Finite experimental photon energy resolution has to be taken into account by an additional convolution with a Gaussian. A typical $L_{2,3}$ absorption spectrum is shown in the bottom panel of Fig. 1.2. It is seen that the absorption signal related to transitions into empty $3d$ states shows up as two peaks at the energetic positions of the $2p_{1/2}$ and $2p_{3/2}$ states, whereas transitions into unoccupied s, p states give rise to a step-like background. Since the magnetic moment of the $3d$ transition metals is mainly governed by $3d$ valence electrons, the latter is usually subtracted as a step function with relative step heights of 2:1 [37], according to the occupation of the $2p_{3/2}$ and $2p_{1/2}$ core states, as shown in the bottom panel of Fig. 1.2.

If $2p \rightarrow 3d$ transitions are excited by circularly polarized radiation, these transitions exhibit a spin polarization because of selection rules [38]. In other words,

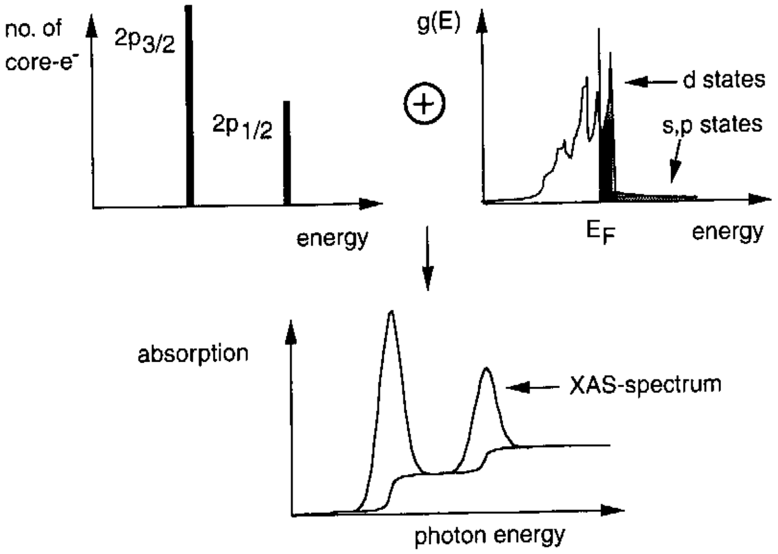

Fig. 1.2. Schematic explanation of X-ray absorption spectroscopy (XAS). The absorption spectrum shown in the bottom panel results from the convolution of the occupied density of states of the core levels (*upper left*) and the unoccupied density of states $g(E)$ of the valence states (*upper right, shaded area*). The contribution from s, p states is usually approximated and subtracted in the form of a step function (*bottom panel*)

for a certain light helicity, more electrons of one spin direction with respect to the direction of the incoming light are excited into the unoccupied $3d$ states than of the other spin direction. In a paramagnet, this does not lead to a change in absorption intensity, since the number of unoccupied states is equal for both spin directions. In a ferromagnet, however, the density of unoccupied states is different for electrons of spin parallel or antiparallel to the magnetization direction, leading to a spin magnetic moment defined by the difference in occupation. This is explained in Fig. 1.3. It shows a schematic representation of the spin resolved density of states, separated into density of states of majority spin electrons at the top and density of states of minority spin electrons at the bottom. If magnetization and light incidence are aligned with each other to some degree, there are consequently more possible transitions for one direction of light helicity than for the other. This leads to a difference in absorption for opposite light helicity. In a dichroism spectrum, calculated as the difference between absorption spectra for opposite helicity, a non-zero difference will show up at the energy positions of the peaks related to transitions from the $2p_{3/2}$ and $2p_{1/2}$ levels into the empty $3d$-like states. Since the spin polarization of $2p_{3/2} \rightarrow 3d$ transitions has an opposite sign than that of the spin polarization of $2p_{1/2} \rightarrow 3d$ transitions [12,35], the dichroism at the L_3 and L_2 edge will have an opposite sign, i.e., the difference curve will show peaks of opposite sign at the energy positions of the L_3 and the L_2 edge. This is shown schematically for the (hypothetical) case of a material with only a spin moment μ_S in the top panel of Fig. 1.4. There, the difference curve between absorption spectra taken with opposite helicity of the circularly polarized light is depicted, which exhibits a positive peak at the L_3 edge, a negative peak at the L_2 edge, and zero elsewhere. The spin polarization of $2p_{1/2} \rightarrow 3d$ transitions is twice

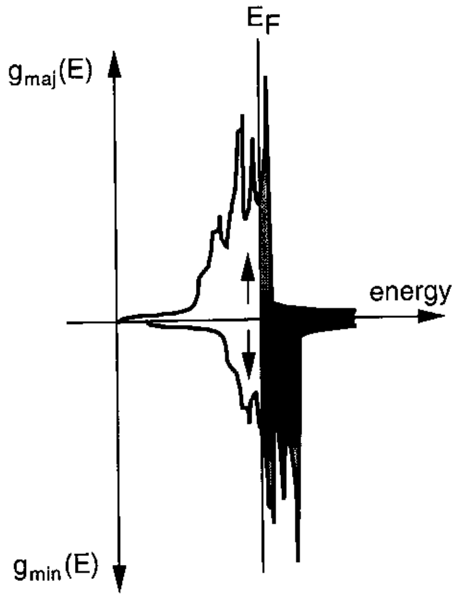

Fig. 1.3. Schematic representation of density of states of a ferromagnetic metal. Shown is the spin resolved density of states for majority electrons $g_{\mathrm{maj}}(E)$ in the positive y direction, and the spin resolved density of states for minority electrons $g_{\mathrm{min}}(E)$ in the negative y direction. The shaded areas are unoccupied density of states above the Fermi energy E_{F} available for $2p \rightarrow 3d$ transitions

as large as the spin polarization of $2p_{3/2} \rightarrow 3d$ transitions. On the other hand, the absorption at the L_3 edge is twice as high as at the L_2 edge because of core hole occupation (cf. Fig. 1.2). Together both lead to an equal size of the dichroism at the two edges, as schematically plotted in the topmost panel of Fig. 1.4.

$2p \rightarrow 3d$ transitions excited by circularly polarized radiation are not only spin polarized, but also show an orbital "polarization." This is a direct consequence of the absorption of a circularly polarized photon with angular momentum $\Delta m = \pm 1$ [12,35]. Both the $2p_{1/2} \rightarrow 3d$ and $2p_{3/2} \rightarrow 3d$ transitions show the same sign and same magnitude of orbital polarization. If a sample possesses a non-zero orbital magnetic moment, this means that the unoccupied states (and also the occupied states) have a non-zero net angular momentum. Let us consider the (hypothetical) case of a metal with only an orbital moment and no spin moment. In this case, there will again be a non-zero dichroism at the L_3 and L_2 edges, but this time with an equal sign at the two edges. Because of the different number of $2p_{1/2}$ and $2p_{3/2}$ electrons, the resulting dichroism at the L_3 edge is twice as large as at the L_2 edge (middle panel of Fig. 1.4).

A real sample will have both spin and orbital magnetic moments. The two extreme cases shown in the top and center panels of Fig. 1.4 define an orthonormal basis for the measured XMCD spectrum from a real sample (bottom panel of Fig. 1.4), which will be a superposition of both. The experimental spectrum can thus be decomposed unambiguously into its spin and orbital basis functions. This is what is done by the so-called sum rules [31,32].

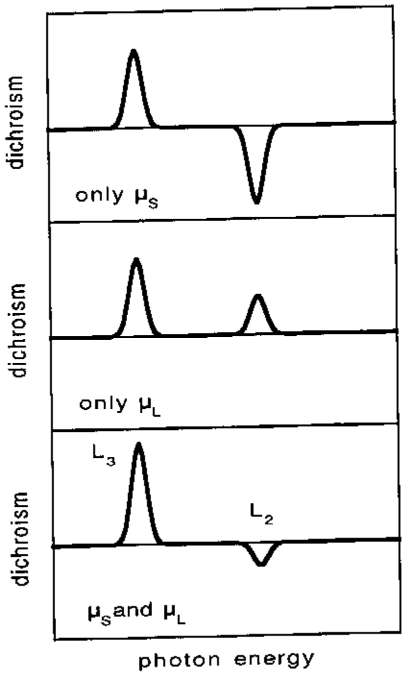

Fig. 1.4. Schematic explanation of sum rule analysis of XMCD spectra to obtain spin and orbital moments. Shown is the decomposition of an XMCD spectrum (*bottom*) into its components resulting from spin moment μ_S (*top*) and orbital moment μ_L (*center*)

It has to be mentioned that what is extracted as the "spin moment" from the sum rules is an effective spin moment $\mu_{S,\mathrm{eff}}$ [32], which includes the actual spin magnetic moment μ_S plus a contribution from the magnetic dipole term. The latter is zero in the bulk of cubic crystals, but can be of the same order as the orbital moment in ultrathin films [39].

Although the derivation of the sum rules was done under simplifying assumptions, and there has been some dispute about their applicability [34,37,40–43], they seem to yield reasonable results for the 3*d* transition metals [34,37,44–46]. Together with the element-selectivity of X-ray absorption spectroscopy at core level absorption edges they provide a quite powerful tool for the quantitative investigation of magnetic materials.

1.2.2 Photoelectron Emission Microscopy

Photoelectron emission microscopy (PEEM) belongs to the parallel imaging electron microscopies. The name "photoelectron" is due to its use in metallurgy in early years, when threshold excitation of photoelectrons at the vacuum level by illumination with Hg discharge lamps was used for the acquisition of work function contrast images [47]. For excitation with higher photon energies, which will be considered in this chapter, low energy secondary electrons are dominant in the imaging process. We nevertheless stick to the name PEEM, although in that case "secondary electron emission microscope" would be more correct.

After the introduction of ultrahigh-vacuum compatible instruments [48, 49], PEEM has been used for the study of surfaces and surface reactions [50–53]. Incorporating a magnetic electron beam splitter allowed the excitation by low energy electrons (LEEM, low energy electron microscopy [25, 54]), which yields additional information about the surface structure and morphology. LEEM can also be employed for magnetic imaging if spin-polarized electrons are used; this is described in Chap. 6. The availability of synchrotron light sources for excitation with X-rays of tunable energy opened a new field of application for PEEMs [55], in which resonant X-ray absorption at elemental core levels is used to image the distribution of different elements at the sample surface.

In a PEEM, in contrast to transmission electron microscopy, the electrons that are used for the imaging do not have a well-defined energy and momentum. To get a sharp image it is therefore necessary to limit the range of electron energies and emission angles. In a PEEM, this is achieved by passing the accelerated electrons through a pinhole aperture, the so-called contrast aperture. A higher lateral resolution is thereby achieved at the expense of intensity, and vice versa.

Figure 1.5 shows the schematic setup of an electrostatic PEEM [21]. The principle of other electrostatic PEEMs is similar, so the main points can be explained using

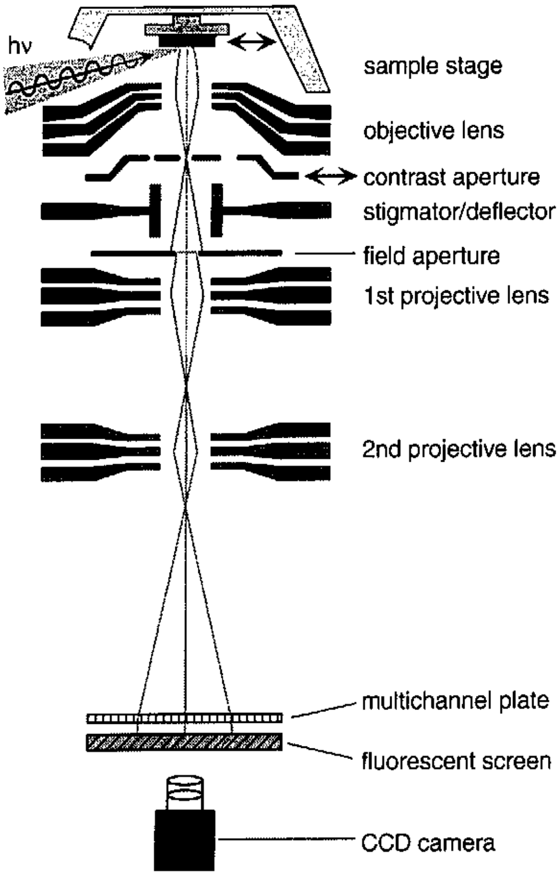

Fig. 1.5. Schematic set up of a photoelectron emission microscope (PEEM). Electrostatic electron lenses create an image of the electrons emitted at the sample surface at a fluorescent screen. (Reproduced from [21] with permission, Copyright (1998) by the World Scientific Publishing Company)

this type. In Fig. 1.5, the sample is shown at the top. It is illuminated by synchrotron radiation under a grazing angle to the sample surface, which is 30 °C in the present example. The sample is kept on ground potential, and electrons are accelerated toward the objective lens, an electrostatic tetrode lens. Typical acceleration voltages are 10–20 kV. The contrast aperture is located in the back focal plane of the objective lens. It selects only those electrons for imaging that originate from a certain range of emission angles. The size and lateral position of this aperture can be changed by moving a slider assembly carrying several apertures of different diameters. In an alternative design, the contrast aperture is located at the back focal plane of the first projective lens [23]. Astigmatism and small misalignments of the optical axis, caused, for example, by a misalignment of the sample, can be corrected by an electrostatic octupole stigmator and deflector. A variable field aperture in the image plane of the objective lens allows one to limit the field of view and to suppress stray electrons. Two electrostatic projective lenses transfer the image onto an imaging unit – which in our example consists of an electron multichannel multiplier and a fluorescent screen on the vacuum side – and charge coupled device (CCD) camera with a conventional lens optics outside the vacuum chamber. Alternative approaches use a glass fiber coupling between the screen and CCD camera [23].

Resolutions down to 20 nm in PEEM imaging using topographic or elemental contrast in threshold photoemission [56] and for excitation with synchrotron radiation [23, 57] have been reported. Even better resolution can be achieved in the LEEM mode, using magnetic objective lenses [25, 26, 58]. Presently, attempts are underway to push the resolution to below 5 nm by aberration correction [59]. In XMCD-PEEM magnetic microspectroscopy, however, intensity is a critical issue. To achieve reasonable acquisition times for the measurement of a complete microscopic and spectroscopic data set, lateral resolution will typically be selected to be a few hundred nanometers in practical microspectroscopy applications.

1.3 About Doing XMCD-PEEM Microspectroscopy

When employing magnetic dichroism effects for the spectroscopy of magnetic materials, the magnetic information is obtained from changes in the spectra that occur either upon changing the magnetization state of the sample or the polarization properties of the exciting radiation. This usually involves the measurement of relatively small differences between large signals and imposes high experimental requirements with respect to signal reproducibility, stability, and flux normalization. The additional imaging step in microspectroscopy is certainly not facilitating the fulfillment of these requirements. In the following, some of the crucial obstacles and their solutions specific to XMCD-PEEM microspectroscopy will be discussed.

1.3.1 Experiment

Let us first consider effects related to the incident radiation. The normalization to the flux of the incoming beam is not straightforward in microspectroscopy, in contrast to conventional absorption spectroscopy. In the latter, usually the photo yield from a suitable optical element in the beamline or from a specially designed flux monitor is recorded simultaneously to the sample signal. Since the entire photon beam is contributing to both the monitor signal and the signal from the sample, normalization is achieved by simply dividing one by the other. In imaging microspectroscopy, however, the *local* photon flux density is important, not the *integral* flux. It cannot be directly measured and may locally deviate significantly from the integral monitor flux signal. The cause of such deviations may be the radiation characteristics of the insertion devices used in third-generation synchrotron light sources and beamline X-ray optics. An inhomogeneous distribution of the photon intensity within the imaged area on the sample invalidates the normalization to a conventional beam monitor. The fact that the intensity distribution of undulators depends also on the relative photon energy with respect to the maximum of the undulator harmonics complicates matters further. Although in principle these effects cannot be avoided, it is possible from the experimental side to reduce the discrepancy between the local flux density and the integral flux measured by the monitor as much as possible, as described in the following. If the remaining error is below a few percent, it can be approximately corrected out in the course of data analysis, as will be explained in more detail in Sect. 1.3.2.

To get a better correlation between the local and integral photon flux it is important that the illuminated area on the sample be not much bigger than what is imaged in microspectroscopy. All the flux outside the field of view adds an irrelevant contribution to the monitor signal. Attention should also be paid to the adjustment of the imaged area to the center of the undulator radiation. Finally, a significant reduction in photon energy-dependent effects can be achieved when the movement of the insertion device gap can be synchronized with the scanning of the grating of the monochromator.

Local energy resolution is an important issue for those beamline optics where the light spot is an image of the exit slit. In such beamlines, the monochromator energy dispersion at the position of the exit slit is imaged onto the sample surface. As a consequence, the local resolution does not change when the slit size is varied. The more serious implication for microspectroscopy is that there is also photon energy dispersion across the image in this case. If the energy dispersion across the image is of comparable size compared to the width of the spectral features of the sample, this shift in energy across the image has to be considered in data analysis of the microspectra.

A point that is normally not given closer attention in microscopy, but which becomes essential in quantitative microspectroscopy, is the linearity of the image detection system. A typical detection system may consist of several components, for example, a multichannel electron multiplier, fluorescence screen, and CCD camera. Although it is desirable to reach intensities as high as possible to get short exposure and scan times, it may sometimes be necessary to sacrifice some output signal in order to operate in the linear range of the image detection system. This range can be determined beforehand by manipulating the incident beam flux in a controlled way and comparing image intensity and flux monitor signal.

1.3.2 Data Analysis

In principle, data analysis in microspectroscopy could follow the same procedures as already established for data analysis in conventional spectroscopy. The main difference, however, is that in imaging microspectroscopy there are *many* spectra, for example, as many as there are pixels in the image. Data analysis for extracting the important parameters from this large number of spectra should therefore meet the following two requirements: It should be quick, and it should be automatic. In this section, a method will be described that allows the automatic analysis of XMCD microspectra to extract spin and orbital magnetic moments by means of sum rules.

To explain the procedure, the example of XMCD-PEEM microspectroscopy from a trilayer of 1.2 atomic monolayers (ML) Ni, an Fe layer of varying thickness, and 6 ML Co on a Cu(001) single crystal surface will be examined [60]. Circularly polarized X-rays of opposite helicity were provided by one of the two helical undulators of beamline BL25SU of SPring-8, Japan. Single pixel spectra corresponding to $3 \times 3\,\mu\text{m}^2$ areas of the sample have been acquired, which have to be analyzed automatically using the sum rules.

A problem for the automatic data analysis is that the data can sometimes be rather noisy, especially at positions where the dichroism is small. In most cases when the sum rules are applied the goal is only to extract two numbers, namely, the spin and orbital moments. In the following, a method is described that makes use of the fact that usually the line shape of the helicity-averaged absorption spectrum does not change across a microscopic image. In this case, the full spectral information of the single-pixel spectra can be reduced to two parameters of interest by a simple fit procedure, thereby improving statistics.

For this procedure, first a template XMCD spectrum with a sufficiently good statistics for sum-rule analysis is generated by averaging many single-pixel spectra over a larger area. This averaged spectrum can be analyzed as described in Sect. 1.2.1. The resulting difference curve between the two spectra for opposite helicity is then cut into two parts at an energy between the L_3 and L_2 edges, such that the two parts represent the dichroism of the L_3 and L_2 absorption edges, respectively. All the single pixel spectra are first corrected for local photon flux effects using a linear correction as a function of photon energy, as described in [60], which is less than 5% of the raw intensity in the present example, and then normalized to an edge jump of one. The two parts of the template XMCD curve are then fit to the single pixel difference curve by simply scaling. The only two fit parameters in that fit are the two scaling factors needed at the L_3 and L_2 edges to reproduce the single pixel difference curve by the template difference curve. An example is shown in Fig. 1.6. It shows corrected Fe $L_{2,3}$ absorption spectra of three different $3 \times 3\,\mu\text{m}^2$ pixels, obtained from 1.2 ML Ni/x ML Fe/6 ML Co films on Cu(001) for different Fe layer thicknesses x [60]. Depicted are the data for incident light of positive (solid line) and negative helicity (dotted line). The two peaks correspond to the Fe L_3 and L_2 absorption maxima. The results obtained from that sample will be discussed in Sect. 1.4.1. The three spectra presented in Fig. 1.6 have been selected to show very different Fe magnetic moments. In the top row (panels (a), (c), and (e)), the single pixel absorption spectra for positive

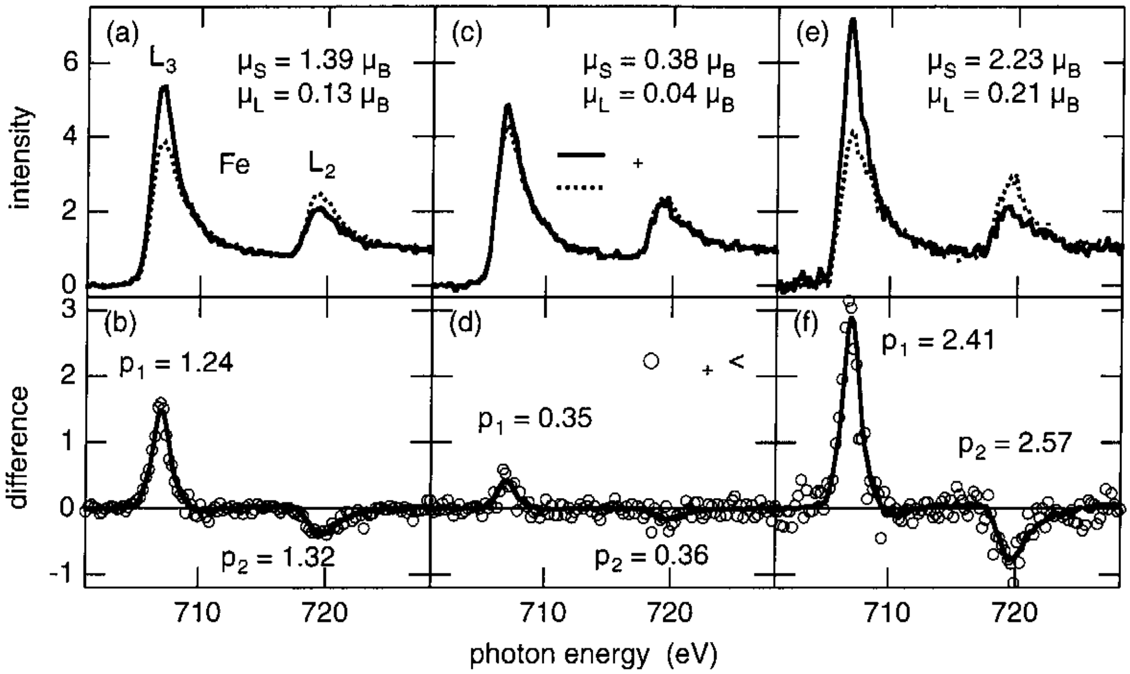

Fig. 1.6. Example for the sum-rule analysis of single pixel spectra. (**a**), (**c**), (**e**): single pixel absorption spectra for positive (*solid lines*) and negative helicity (*dotted lines*) from 1.2 ML Ni/Fe/6 ML Co/Cu(001) films for three different Fe thicknesses ((**a**) 10 ML, (**b**) 5 ML, (**c**) 2 ML). (**b**), (**d**), (**f**): difference between spectra for opposite helicity of panels (**a**), (**c**), and (**e**) (open symbols). The solid lines in (**b**), (**d**), and (**f**) are portions of a template difference curve, obtained from averaging over a larger area, scaled by the fit parameters p_1 and p_2 at the L_3 and L_2 edges, respectively, to match the single pixel data. The spin and orbital moments, calculated from p_1, p_2, and the spin and orbital moments of the template spectrum, are listed in panels (**a**), (**c**), and (**e**). (Reproduced from [60] with permission, Copyright (2001) by Elsevier Science)

(solid line) and negative helicity (dotted line) are shown. The bottom panels (b), (d), and (f) show the corresponding single pixel difference curves as open symbols. Please note the different vertical scale in the top and bottom panels. The solid lines in panels (b), (d), and (f) are the result of the template fits described above. The corresponding scaling factors for the dichroism at the L_3 and L_2 edges, p_1 and p_2, respectively, are also given. The solid line is, in other words, identical to the difference curve of the template spectrum, scaled by p_1 at the L_3 edge and by p_2 at the L_2 edge. The analysis of the template spectrum resulted in a spin moment of 1.1 μ_B and an orbital moment of 0.1 μ_B [60]. From these moments and the knowledge of p_1 and p_2, it is straightforward to calculate the spin and orbital moments for each of the single pixel fit results. For the three pixels presented in Figure 1.6, the resulting Fe moments are listed in the upper panels.

By this template fit procedure, stable fits are obtained even for noisy single pixel data and small dichroism. The scatter of individual data points in the difference spectrum is averaged out in an elegant way. Furthermore, the position of the zero line is maintained, and data points far outside the absorption edges are not considered in the fit. However, several positions of the image should be checked to make sure that the prerequisite for the fit, namely, the constant shape of the helicity-averaged absorption spectrum, is fulfilled.

1.4 Specific Examples

We will now discuss two specific examples in which the application of XMCD-PEEM microspectroscopy has proven beneficial to the study of the involved physical phenomena.

1.4.1 Ultrathin fcc Fe Films

Interesting systems for quantitative analysis of magnetic moments from microspectroscopy are ultrathin epitaxial Fe films. In these films, the interplay between structural and magnetic properties leads to a variety of different structural and magnetic phases. Whereas bulk Fe exists only in the bcc structure at temperatures up to 1,184 K, an fcc-like phase of Fe can be stabilized at room temperature when grown epitaxially on substrates with suitable surface lattice dimensions [61–71]. Room-temperature-grown films of Fe on Cu(001) single crystal surfaces are known to exhibit three structurally and magnetically different phases, depending on film thickness. For thicknesses below 4 atomic monolayers (ML), a fully ferromagnetic tetragonally expanded fcc-like structure is present (phase I) [62, 63]. In the thickness range between 4 and 11 ML, a second phase (II), a relaxed fcc structure, is found, in which one observes a non-ferromagnetic behavior of the inner film layers [64–66]. For thicknesses above 11 ML, a third phase appears, a ferromagnetic (011)-oriented bcc phase (III) [67–69]. The magnetic behavior of these three phases is linked to the structure by the atomic volume. For different atomic volumes different magnetic ground states are theoretically predicted [72–74].

Especially the second phase of fcc Fe, where a large fraction of the film is non-ferromagnetic, has attracted a lot of interest. An antiferromagnetic coupling between ferromagnetic layers, separated by phase II fcc Fe, has been concluded from the measurements of magnetization loops of Co/Fe/Co/Cu(001) [75, 76] and Ni/Fe and $Ni_{81}Fe_{19}$/Fe multilayers [77, 78]. While total magnetization measurements of stacks of multiple magnetic layers can give only indirect evidence about the magnetic configuration, XMCD-PEEM microspectroscopy can provide element-resolved quantitative information. In this section, measurements of a Ni/Fe/Co/Cu(001) sample are presented [79], in which microspectroscopy at the Fe $L_{2,3}$ edges was used for determining the magnetic moments of the Fe layer. Element-resolved imaging of the Co underlayer and Ni overlayer revealed the presence of antiferromagnetic interlayer coupling.

To study the thickness dependence by microspectroscopy, the Fe and Ni layers were shaped into 255-μm-wide crossed wedges. They were prepared by placing a slit aperture of 0.5-mm width 1 mm in front of the sample and rocking the sample-slit assembly by ±7.5 ° about the long axis of the aperture during deposition. The thickness of the continuous Co underlayer was 6 ML, the Fe thickness 0–14 ML, and the Ni thickness 0–6 ML. Low magnification settings of the PEEM enabled imaging of a complete wedge.

Fig. 1.7 shows magnetic images of the Co and Ni layers at the onset of the crossed Ni and Fe wedges. The complete Fe wedge of 0–14 ML Fe is within the imaged area. The Fe thickness increases from right to left, as indicated at the upper axis. The imaged part of the Ni wedge corresponds to 0–4 ML thickness, increasing from top to bottom, as indicated at the right axis. The Fe thickness is such that all three phases, as mentioned above, are present within this wedge. The upper panel of Fig. 1.7 shows the magnetic asymmetry of the Co layer. It shows a nearly uniform bright contrast. It corresponds to a magnetization direction along the direction of the external field, which was applied after the deposition of the Co layer and again after completion of the trilayer. The lower panel shows the contrast obtained at the Ni L_3 edge. Note that here the grayscale is defined to include positive as well as negative values of the asymmetry, in contrast to panel (a). In a stripe located at Fe thicknesses

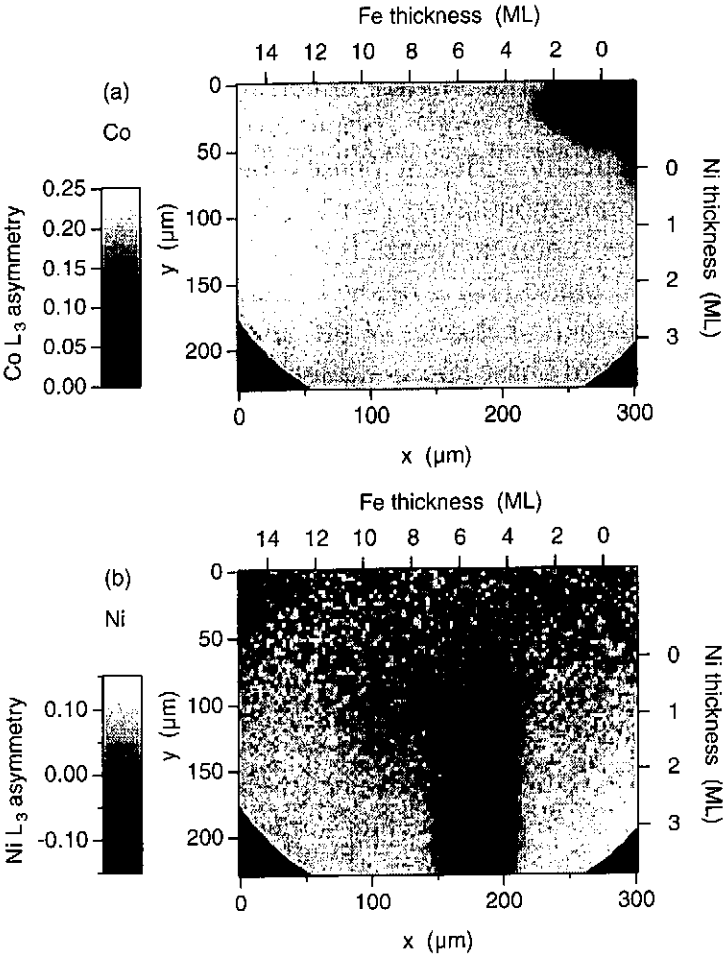

Fig. 1.7. Co (**a**) and Ni (**b**) asymmetry images of 0–4 ML Ni/0–14 ML Fe/6 ML Co/Cu(001). Ni and Fe thicknesses are indicated at the right and top axes, respectively. Different levels of gray correspond to different values of the magnetic asymmetry, as explained in the legend. Note that in panel (**b**) zero corresponds to an intermediate grayscale level, in contrast to panel (**a**), where zero is black. The Ni magnetization is antiparallel to the Co magnetization around 5 ML Fe thickness. (Reproduced from [79] with permission, Copyright (2000) by Elsevier Science)

between 5.0 and 6.5 ML, a negative (dark) Ni asymmetry is found, while the rest of the image exhibits an approximately uniform positive (bright) contrast. A negative asymmetry corresponds to an antiparallel orientation of the Ni layer magnetization at this position with respect to the Co layer magnetization. The Fe layer, consequently, mediates an antiferromagnetic interlayer coupling between the Co and Ni layers at this particular Fe thickness.

We will now turn our attention to the laterally resolved quantitative evaluation of the Fe magnetic moments at exactly the same region of the sample by XMCD-PEEM microspectroscopy. The result of a pixel-by-pixel sum-rule analysis is shown in the upper panel of Fig. 1.8. A total of 121 images for each helicity were recorded as a function of photon energy in the interval between 701 and 728 eV, similar to the spectra shown in Fig. 1.6. The size of a single pixel is $3 \times 3\,\mu\text{m}^2$, the exposure time was 10 s per image. Different levels of gray correspond to different values of the Fe effective spin moment, as explained in the legend. In the upper part of the image at zero or low Ni coverage the three different phases of Fe, as introduced above, are recognized by their distinctly different spin moments. They are labeled I, II, and III. Phase I extends up to a Fe thickness of approximately 3.5 ML and shows high spin moments of up to 2.5 μ_B. Phase II between approximately 3.5 and 11 ML is characterized by a low spin moment, whereas phase III again shows increasing spin moments up to 2.0 μ_B at Fe thicknesses above 11 ML. These numbers can be seen more easily from a line scan along the Fe wedge. The open symbols in Fig. 1.8 (b) represent a horizontal line scan obtained from a 7 pixel vertical average of the uncovered Fe/6 ML Co/Cu(001) sample in the region indicated by the upper white rectangle in panel (a). For increasing thickness of the Ni top layer, differences in phase II Fe moment are observed. The solid symbols of Fig. 1.8 (b) show a line scan

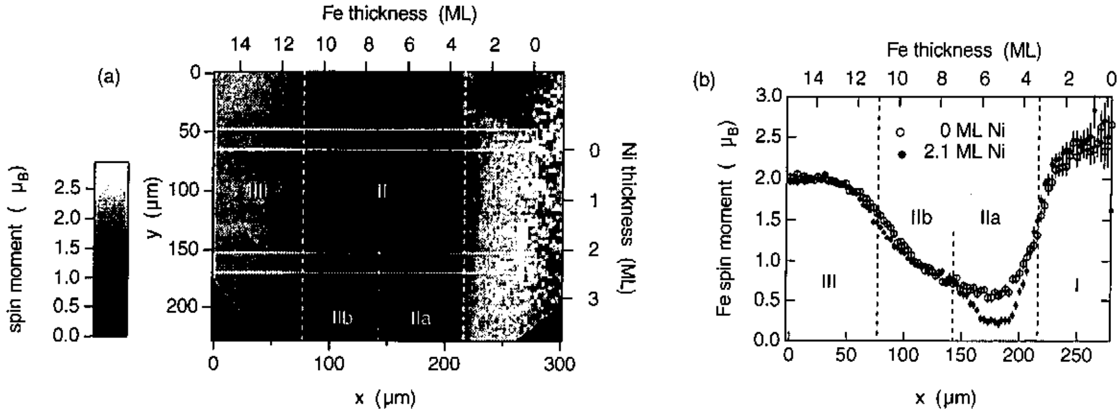

Fig. 1.8. (**a**) Result of a pixel-by-pixel sum-rule analysis for the Fe effective spin moment $\mu_{S,\text{eff}}$. Different values of $\mu_{S,\text{eff}}$ are represented by different levels of gray, as explained in the legend. The imaged region of the crossed Ni/Fe double wedge is exactly the same as in Fig. 1.7. Ni and Fe thicknesses are indicated at the right and top axes, respectively. Regions with different values of $\mu_{S,\text{eff}}$ are separated by dashed vertical lines and labeled I through III, IIa, and IIb. Horizontal line scans of $\mu_{S,\text{eff}}$ at the positions indicated by white rectangles in (**a**) are shown in (**b**). (Reproduced from [79] with permission, Copyright (2000) by Elsevier Science)

at around 2.1 ML Ni thickness (lower rectangle in panel (a)). From this line scan and also from the image plot of the Fe spin moments in panel (a) a further reduction of the Fe moment in phase II between about 4 and 7 ML compared to the uncovered Fe layer is observed. This region is labeled IIa, to distinguish it from the rest of phase II, where no change as a function of Ni overlayer thickness occurs (region IIb).

The observed Fe moments in phase I and III agree rather well with what is expected and known from literature [46, 80]. The interesting behavior occurs in phase II. There is some dispute in the literature about the origin and location of the remaining moment of about 0.7–1.0 μ_B in phase II of the uncovered Fe/Co/Cu(001) sample: While from oxygen adsorption [75, 76] and XMCD experiments [81, 82] it had been concluded that the surface is not ferromagnetically ordered, and the ferromagnetism, consequently, had been attributed to the Co/Fe interface, other XMCD experiments [80], as well as measurements of photoelectron diffraction in magnetic dichroism [83] and spin-resolved valence band photoemission [84], provided evidence for the presence of a ferromagnetic layer on top of non-ferromagnetic underlayers, plus possibly ferromagnetism at the Fe/Co interface. The result from XMCD-PEEM microspectroscopy has to be interpreted as the exponentially depth averaged signal of all Fe monolayers in the film. A constant amount of ferromagnetic Fe at both interfaces plus non-ferromagnetic Fe in between would lead to a decreasing apparent magnetic moment with increasing Fe film thickness. This is not observed in the experiment (cf. Fig. 1.8). The situation is, therefore, probably more complicated. Layer-wise or bilayer-wise antiferromagnetic ordering of Fe moments [85–88], frustrations at interface steps or non-collinear moments [89] may have to be considered, possibly supported by further theoretical calculations.

By comparing Fig. 1.7 and Fig. 1.8, it becomes evident that region IIa with the extremely low Fe moment corresponds to the region of antiferromagnetic coupling between Ni and Co. Assuming ferromagnetic interface layers at both interfaces, this lowering of Fe moments could be explained by the strong direct coupling to the neighboring magnetic layers. In the case of antiferromagnetic alignment of Co and Ni, the Fe layers at both interfaces should be aligned opposite to each other, leading to lower apparent moments compared with the parallel alignment in region IIb. The question remains why without Ni overlayer no such decrease of the Fe moment by antiparallel alignment of the ferromagnetic Fe surface layer to the Co layer (and thus also to the Fe interface layer) is observed at the same Fe thickness. The reason could be some different influence of interface roughness and roughness-related magnetic frustrations in Fe/Co with and without Ni overlayer. There is also the possibility that without Ni, a 90 °C orientation of the Fe surface layer around 5.5 ML Fe thickness is present as the result of such competing frustrations, similar to the mechanisms leading to 90 °C interlayer exchange coupling [90, 91].

In the present example of Ni/Fe/Co trilayers, XMCD-PEEM microspectroscopy was used for the thickness-dependent study of Fe moments. The effective spin moments of Fe in the three structural phases could be obtained from images showing the moments in a two-dimensional plot as a function of both Ni and Fe thicknesses. Characteristic changes connected with antiferromagnetic interlayer exchange coupling across the Fe layer could be observed. For this purpose, no special lateral resolution is required. In that case, microspectroscopy is just used as a very efficient way of parallel acquisition of a great number of XMCD spectra of crossed double wedges designed at length scales that are convenient for imaging with respect to intensity and lateral resolution. In the next section, an example of microspectroscopy with higher resolution is presented in which spin and orbital magnetic moments within magnetic domains are determined.

1.4.2 Spin Reorientation Transition in Co/Ni Bilayers

The control of the easy axis of magnetization is important for many applications in which magnetic ultrathin films are used. The direction of the easy axis is described by the angle-dependent part of the free energy, the so-called magnetic anisotropy energy (MAE). Minimization of the MAE with respect to the magnetization direction yields the easy axis of magnetization. The MAE is directly related to the anisotropy of the orbital magnetic moment [92]: The orbital moment should be higher for a direction of magnetization preferred by the MAE. This can be used to measure the angle dependence of the MAE in an element-selective and laterally resolved way by mapping the orbital magnetic moment by XMCD-PEEM microspectroscopy.

In the example presented in this section, Co/Ni epitaxial bilayers on Cu(001) have been investigated [93]. They were shaped into wedges of 255-μm widths, rotated by 90 °C to each other, similar to the wedges described in the previous section. Co and Ni single films on Cu(001) exhibit a different behavior with respect to the easy axis of magnetization: Whereas Co/Cu(001) is always magnetized in the film plane ("in-plane") [94, 95], Ni/Cu(001) shows a perpendicular magnetization ("out-of-plane") over a wide range of thicknesses [96–99]. In Co/Ni bilayers, in-plane magnetization is, therefore, expected for large Co thicknesses and small Ni thicknesses, whereas out-of-plane magnetization should be present for small Co thicknesses and large Ni thicknesses.

Figure 1.9 shows the result of a pixel-by-pixel sum-rule analysis of the Ni spin moments of a region in a Ni/Co/Cu(001) crossed double wedge. The Ni thickness increases in the displayed area from 10.7 to 14 ML from left to right, as indicated at the top axis, and the Co thickness increases from 1.35 to 2.65 ML from bottom to top, as indicated at the right-hand axis. The image was obtained from 76,800 single pixel XMCD spectra of $370 \times 370\,\mathrm{nm}^2$ size each. The resolution of the PEEM was adjusted to 500 nm, which resulted in a 30 s exposure time per photon energy step. A total of 105 images for each helicity between 845 and 890 eV photon energy were acquired using variable photon energy step spacings of 0.26 eV near the L_3 peak, 0.34 eV near the L_2 peak, 0.65 eV before the L_3 peak and in between the L_3 and L_2 peaks, and 1.4 eV in the post-L_2 region. Unlike the previous example, this sample was not magnetized by an external field before imaging. The resulting moments, therefore, include the cosine of the angle between the helicity of the incoming light and the local magnetization direction, which is different in the different domains of the as-grown domain structure. The microspectroscopic analysis thus does not yield the absolute moments, but a projection on the direction of incoming light, which, in the present example, was from bottom to top of Fig. 1.9, with an angle of 60 °C to

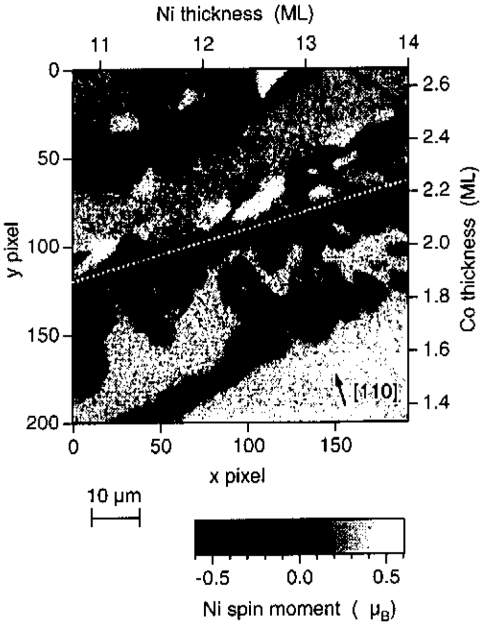

Fig. 1.9. Map of Ni spin moment projections onto the light incidence direction (from bottom to top, with an angle of 30 °C to the sample surface), resulting from the pixel-by-pixel sum-rule analysis of 76,800 single-pixel XMCD microspectra of a Co/Ni/Cu(001) crossed double-wedge sample. The Ni thickness is indicated at the top axis, the Co thickness at the right-hand axis. The grayscale to magnetic moment conversion is given in the legend at the bottom. At the white dotted line a spin reorientation transition between in-plane magnetization (top) and out-of-plane magnetization (bottom) occurs. Arrows in some domains indicate the magnetization directions. (From [93], Copyright (2000) by the American Physical Society)

the surface normal. Note that the grayscale used to represent the Ni spin moment projections is symmetric around zero.

Inspection of the domain pattern of Fig. 1.9 reveals two qualitatively different regions separated by the dotted line. In the upper part of the image, four different shades of gray are recognized, namely black, dark gray, light gray, and white. In the lower part, only two different shades of gray are found and the domains are more rounded. Quantitative analysis of the values of $\mu_{S,\mathrm{eff}}$ for Ni in the single domains leads to the result that in the upper part of the image the magnetization direction is in-plane, oriented along the four <110> crystallographic directions, as indicated by arrows. Since the light incidence azimuth was deliberately rotated out of the crystal symmetry axes, each of these four directions results in a different grayscale representation. In the lower part of the image, the magnetization is out-of-plane, either parallel or antiparallel to the surface normal. The resulting absolute value of the Ni effective spin moment is 0.65 μ_B, constant over the entire image [93].

At the dotted line of Fig. 1.9, a spin reorientation transition between in-plane and out-of-plane magnetization occurs, either by varying the Ni thickness, or by varying the Co thickness. From the position and slope of that line, conclusions about the relative MAEs of the Co and Ni layers can be drawn [93]. The domain pattern on the out-of-plane side of the spin reorientation line is related to the spin reorientation transition: As the spin reorientation line is approached, more and more oppositely magnetized out-of-plane domains are formed. This can be explained by the competition between the magneto static energy, on the one hand, and the energy cost for creating domain walls, on the other hand. Closely spaced, alternating up and down magnetized out-of-plane domains have a lower magneto static energy than a single out-of-plane domain due to partial flux closure [100]. The formation of domains, on the other hand, requires the creation of additional domain walls of certain domain wall energy. Since in domain walls between two out-of-plane domains an in-plane component of the magnetization is present, this domain wall energy is directly related to the MAE of the system. Close to the spin reorientation transition the domain wall energy is consequently low, so that the formation of many small domains can be energetically favorable [101]. A more detailed discussion of the domain structure at spin reorientation transitions between in-plane and out-of-plane magnetization is given in Chap. 7.

Figure 1.10 shows the result of the pixel-by-pixel sum-rule analysis for the Ni orbital moments of the same region of the sample as Fig. 1.9. The same domain pattern is recognized, although the noise in the image is higher. The higher noise is a consequence of the application of the sum rules, where for the evaluation of the spin moment the peak areas of the L_2 and L_3 dichroism are added, whereas for the orbital moment they are subtracted [31]. The interesting quantity for the interpretation of the orbital moment, independent of magnetization direction, is the ratio of orbital to spin moment, $\mu_L/\mu_{S,\mathrm{eff}}$. From the statistics of Fig. 1.10 it is clear that for the present 370×370 nm^2 pixel resolution a pixel wise interpretation of orbital moments would yield too big an error. To improve statistics in $\mu_L/\mu_{S,\mathrm{eff}}$, the information from

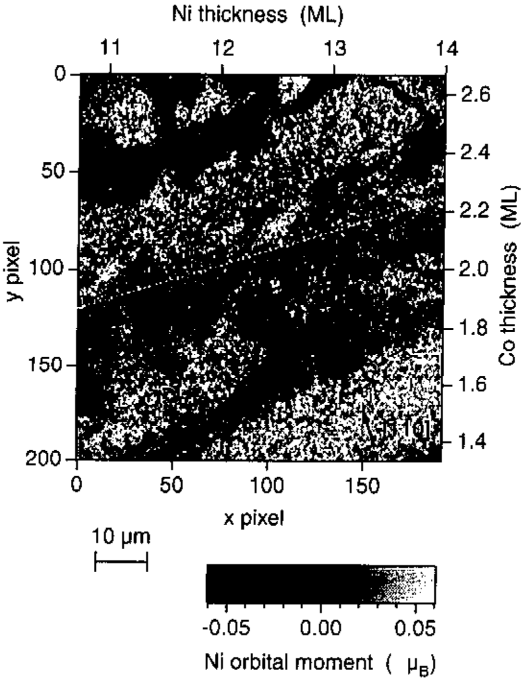

Fig. 1.10. As in Fig. 1.9, but for the Ni orbital moment μ_L. Different projections onto the direction of the incoming light are represented by different grayscales, as defined in the legend. (From [93], Copyright (2000) by the American Physical Society)

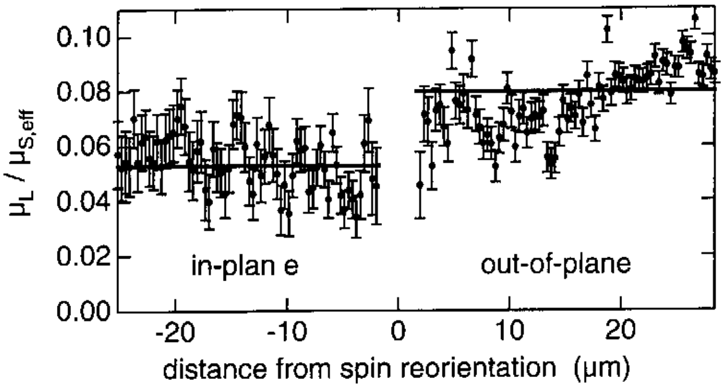

Fig. 1.11. Orbital to spin moment ratio $\mu_L/\mu_{S,\mathrm{eff}}$ as a function of the distance from the spin reorientation line. Each data point is an average of 192 points along a line parallel to the spin reorientation transition in Fig. 1.9. Solid lines mark the average $\mu_L/\mu_{S,\mathrm{eff}}$ ratio in the in-plane region (left) and in the out-of-plane region (right). (From [93], Copyright (2000) by the American Physical Society)

several pixels has to be averaged. The result of an averaging of pixels with a common distance from the spin reorientation line is shown in Fig. 1.11. Here, the orbital to spin moment ratio $\mu_L/\mu_{S,\mathrm{eff}}$ is plotted as a function of the distance from the spin reorientation line. The left-hand side of Fig. 1.11 corresponds to the in-plane region of the image, the right-hand side to the out-of-plane region. Each data point contains information of 192 pixels along a line parallel to the spin reorientation transition. The horizontal solid lines in Fig. 1.11 mark the average on both sides.

Although there is still considerable scatter, the orbital moment in the out-of-plane region is seen to be distinctly higher than in the in-plane region by nearly 0.03 $\mu_{S,\mathrm{eff}}$. This is interpreted in terms of the above-mentioned connection between the anisotropy of the orbital moment and the magnetic anisotropy energy. In the present example of Co/Ni/Cu(001), the MAE of the Ni layer alone is favoring an out-of-plane easy axis in the whole range of thicknesses considered here [93]. The observed in-plane magnetization is thus exclusively due to a stronger in-plane anisotropy of the Co layer, which overcompensates for the out-of-plane anisotropy of the Ni layer. The rigid magnetic exchange coupling between the two magnetic layers leads to a common easy axis of the bilayer, which results from the energy minimization of the summed MAE contributions of both layers. That means that in the upper part of the images the magnetization direction of the Ni layer is along the Ni hard in-plane direction, and in the lower part along the Ni easy out-of-plane direction. The Ni orbital moment is thus higher for a magnetization direction along the easy axis and lower for a magnetization direction along the hard axis.

Estimates for the size of the MAE can be made from the difference in orbital moment. A simplified theoretical description of the relation between the difference in orbital moment and the difference in MAE for two different magnetization directions resulted in a proportionality between both [92]. The proportionality factor, however, depends on some integrals over density of states in the valence bands [92] and may vary strongly between different samples, or even as a function of film thickness. In the present example, the change in orbital moment is 0.027 $\mu_{S,\mathrm{eff}}$, or 0.018 μ_B. The proportionality constant between $\Delta\mu_L$ and MAE has been determined experimentally for Ni in Ni/Pt multilayers by independent measurements of both the orbital moments and the magnetic anisotropy [102]. Assuming that the same proportionality constant is valid for the present Co/Ni bilayers, an MAE of $+(47 \pm 10)$ μeV/atom is obtained. In spite of the uncertainties connected to the use of the proportionality constant of a different sample, this value very well makes sense if we remember that XMCD measures the exponentially depth weighted average of the orbital magnetic moment within the probing depth and, thus, of the MAE. A literature value for the MAE of the inner layers of Ni/Cu(001) is +34 μeV/atom [99]. Considering the fact that in the present sample the interface between Ni and Co has been found to contribute a high positive MAE [93], the value of +47 μeV/atom is amazingly close to the expected anisotropy energy of Co/Ni/Cu(001).

In this example of Co/Ni/Cu(001), XMCD-PEEM has been used for a quantitative analysis of the Ni spin moment projections, the characterization of local magnetization directions, and the identification of a spin reorientation transition between in-plane and out-of-plane easy axes in the sample. The observed local moments' projections are consistent with an absolute value of the effective spin moment, which is constant across the imaged area of the sample, and domains with either $\langle 110 \rangle$ in-plane magnetization or $\pm[001]$ out-of-plane magnetization. The connection of orbital moments and magnetic anisotropy adds an important feature to XMCD-PEEM microspectroscopy, which makes it an ideal tool for the study of local magnetic anisotropies in small magnetic structures.

1.5 Summary and Outlook

XMCD in X-ray absorption and PEEM can be combined into imaging XMCD microspectroscopy measurements at a reasonable experimental effort. The PEEM is thereby used as a parallel detector for local electron yield with microscopic spatial resolution. Scanning the photon energy of the incident X-ray beam and recording PEEM images at each energy step allows one to extract the full spectroscopic information inherent to XMCD from every position in the images, if some experimental requirements concerning evenness of illumination, flux normalization, as well as linearity and stability of the image detection system can be fulfilled. Quantitative information about the element-resolved magnetic moments, separated into spin and orbital contributions, can be extracted from a full image XMCD microspectrum through the use of sum rules. In cases where no special microscopic resolution is needed, this can be used for a quick but detailed map of the thickness dependence of thin film samples by microspectroscopy of wedge-shaped samples. This was illustrated by the example of Ni/Fe/Co ultrathin films on Cu(001), where the Ni and Fe layers were grown as crossed double-wedges.

The method can also be used to investigate micromagnetic phenomena by XMCD. The example of XMCD-PEEM microspectroscopy at the spin reorientation transition between out-of-plane and in-plane easy magnetic axes in Co/Ni/Cu(001) showed how the correlation between the anisotropy of the orbital magnetic moment and the magnetocrystalline anisotropy can be used to obtain element-resolved information about local magnetic anisotropy from XMCD microspectra.

Future improvements concerning the brightness of the illumination and the efficiency of the detection system will reduce the noise level of the microspectra and allow one to probe magnetic anisotropy at the microscopic level, for example, in domain walls or in technologically relevant magnetic microstructures. It will also enable one to choose a higher lateral resolution for microspectroscopy, maintaining reasonable acquisition times. The development of new PEEM instruments with aberration-correcting optics [59] will further push the limit for the attainable maximum resolution. Beamlines providing high-brilliance circularly polarized radiation with the possibility of quick helicity reversal [103] will help improve the accuracy of circular dichroism-based techniques.

The use of imaging energy filters [104–107] to select only electrons of a certain kinetic energy for the imaging process has interesting implications for magnetic microspectroscopy. On the one hand, it allows magnetic dichroism effects that occur only in photoemission [108] to be included in a microspectroscopic study. If the projective electron optics is tuned in order not to project the real space image plane onto the screen but the diffraction plane, on the other hand, photoelectron diffraction measurements [109–111] can be combined with XMCD. Positioning of the contrast aperture to certain features in the photoelectron diffraction pattern can then be used to obtain structure-sensitive XMCD microspectroscopy data and, thus, combine structural and magneto-spectroscopic information.

Finally, the inclusion of time-resolved stroboscopic pump-probe experiments that exploit the pulsed time structure of synchrotron radiation [112] into XMCD-PEEM microspectroscopy opens the way for the quantitative investigation of magnetization dynamics on microscopic length scales. Snapshots of the spatial spin and orbital magnetic moments' distribution in the course of reversible dynamic magnetization processes may be obtained in that way.

Acknowledgement. The author would like to thank J. Kirschner, F. Offi, S.-S. Kang, J. Gilles, S. Imada, and S. Suga for discussions and experimental work. Support from BMBF (No. 05 SL8EF1 9), DFG (Nos. Ki 358/3-1 and 446 JAP-113/179/0), JSPS, and JASRI is gratefully acknowledged.

References

1. B.P. Tonner, D. Dunham, T. Droubay, J. Kikuma, J. Denlinger, E. Rotenberg, and A. Warwick, J. Electron Spectrosc. Relat. Phenom. **75**, 309 (1995).
2. L. Casalis, W. Jark, M. Kiskinova, D. Lonza, P. Melpignano, D. Morris, R. Rosei, A. Savoi, A. Abrami, C. Fava, P. Furlan, R. Pugliese, D. Vivoda, G. Sandrin, F.-Q. Wei, S. Contarini, L. DeAngelis, C. Gariazzo, P. Natelli, and G.R. Morrison, Rev. Sci. Instrum. **66**, 4870 (1995).
3. J. Voss, J. Electron Spectrosc. Relat. Phenom. **84**, 29 (1997).
4. M. Kiskinova, Surf. Rev. Lett. **7**, 447 (2000).

5. L. Baumgarten, C.M. Schneider, H. Petersen, F. Schäfers, and J. Kirschner, Phys. Rev. Lett. **65**, 492 (1990).
6. Y. Kagoshima, T. Miyahara, M. Ando, J. Wang, and S. Aoki, J. Appl. Phys. **80**, 3124 (1996).
7. T. Warwick, K. Franck, J.B. Kortright, G. Meigs, M. Morenne, S. Myneni, E. Rotenberg, S. Seal, W.F. Steele, H. Ade, A. Garcia, S. Cerasari, J. Denlinger, S. Hayakawa, A.P. Hitchcock, T. Tyliszczak, J. Kikuma, E.G. Rightor, H.-J. Shin, and B.P. Tonner, Rev. Sci. Instrum. **69**, 2964 (1998).
8. O. Pietzsch, A. Kubetzka, M. Bode, and R. Wiesendanger, Phys. Rev. Lett. **84**, 5212 (2000).
9. M. Kleiber, M. Bode, R. Ravlic, and R. Wiesendanger, Phys. Rev. Lett. **85**, 4606 (2000).
10. A. Hubert and R. Schäfer: Magnetic Domains, Springer, Berlin (1998), and references therein.
11. D. Weller: Magneto-optical Kerr spectroscopy of transition metal alloy and compound films. In: H. Ebert and G. Schütz (ed.), Spin-Orbit-Influenced Spectroscopies of Magnetic Solids, Springer, Berlin (1996).
12. H. Ebert, Rep. Prog. Phys. **59**, 1665 (1996).
13. C.M. Schneider, Z. Celinski, M. Neuber, C. Wilde, M. Grunze, K. Meinel, and J. Kirschner, J. Phys.: Cond. Matt. **6**, 1177 (1994).
14. T. Kinoshita, K.G. Nath, Y. Haruyama, M. Watanabe, M. Yagi, S.-I. Kimura, and A. Fanelsa, J. Electron Spectrosc. Relat. Phenom. **92**, 165 (1999).
15. C.M. Schneider, K. Meinel, K. Holldack, H.P. Oepen, M. Grunze, and J. Kirschner: Magnetic spectro-microscopy using magneto-dichroic effects in photon-induced auger electron emission. In: B.T. Jonker et al. (ed.), Magnetic Ultrathin Films, Materials Research Society, Pittsburgh (1993).
16. C.M. Schneider, K. Holldack, M. Kinzler, M. Grunze, H.P. Oepen, F. Schäfers, H. Petersen, K. Meinel, and J. Kirschner, Appl. Phys. Lett. **63**, 2432 (1993).
17. P. Fischer, T. Eimüller, G. Schütz, P. Guttmann, G. Schmahl, K. Prueg, and G. Bayreuther, J. Phys. D: Appl. Phys. **31**, 649 (1998).
18. J. Stöhr, Y. Wu, M.G. Samant, B.B. Hermsmeier, G. Harp, S. Koranda, D. Dunham, and B.P. Tonner, Science **259**, 658 (1993).
19. W. Swiech, G.H. Fecher, Ch. Ziethen, O. Schmidt, G. Schönhense, K. Grzelakowski, C.M. Schneider, R. Frömter, H.P. Oepen, and J. Kirschner, J. Electron Spectrosc. Relat. Phenom. **84**, 171 (1997).
20. F.U. Hillebrecht, D. Spanke, J. Dresselhaus, and V. Solinus, J. Electron Spectrosc. Relat. Phenom. **84**, 189 (1997).
21. W. Kuch, R. Frömter, J. Gilles, D. Hartmann, Ch. Ziethen, C.M. Schneider, G. Schönhense, W. Swiech, and J. Kirschner, Surf. Rev. Lett. **5**, 1241 (1998).
22. J. Stöhr, H.A. Padmore, S. Anders, T. Stammler, and M.R. Scheinfein, Surf. Rev. Lett. **5**, 1297 (1998).
23. S. Anders, H.A. Padmore, R.M. Duarte, T. Renner, T. Stammler, A. Scholl, M.R. Scheinfein, J. Stöhr, L. Séve, and B. Sinkovic, Rev. Sci. Instrum. **70**, 3973 (1999).
24. T. Kachel, W. Gudat, C. Koziol, T. Schmidt, G. Lilienkamp, E. Bauer, and M. Altman, J. Appl. Phys. **81**, 5025 (1997).
25. E. Bauer, Rep. Prog. Phys. **57**, 895 (1994).
26. E. Bauer, Surf. Rev. Lett. **5**, 1275 (1998).
27. S. Imada, S. Suga, W. Kuch, and J. Kirschner, Surf. Rev. Lett. **9**, 877 (2002).
28. A. Scholl, J. Stöhr, J. Lüning, J.W. Seo, J. Fompeyrine, H. Siegwart, J.-P. Locquet, F. Nolting, S. Anders, E.E. Fullerton, M.R. Scheinfein, and H.A. Padmore, Science **287**, 1014 (2000).

29. F. Nolting, A. Scholl, J. Stöhr, J.W. Seo, J. Fompeyrine, H. Siegwart, J.-P. Locquet, S. Anders, J. Lüning, E.E. Fullerton, M.F. Toney, M.R. Scheinfein, and H.A. Padmore, Nature **405**, 767 (2000).
30. G. Schütz, W. Wagner, W. Wilhelm, P. Kienle, R. Zeller, R. Frahm, and G. Materlik, Phys. Rev. Lett. **58**, 737 (1987).
31. B.T. Thole, P. Carra, F. Sette, and G. van der Laan, **68**, 1943 (1992).
32. P. Carra, B.T. Thole, M. Altarelli, and X. Wang, Phys. Rev. Lett. **70**, 694 (1993).
33. J. Stöhr, J. Electron Spectrosc. Relat. Phenom. **75**, 253 (1995).
34. Y.U. Idzerda, C.T. Chen, H.-J. Lin, H. Tjeng, and G. Meigs, Physica B **208–209**, 746 (1995).
35. H. Ebert: Circular magnetic X-ray dichroism in transition metal systems. In: H. Ebert and G. Schütz (ed.), Spin-Orbit-Influenced Spectroscopies of Magnetic Solids, Springer, Berlin (1996).
36. J. Stöhr and R. Nakajima, IBM J. Res. Develop. **42**, 73 (1998).
37. C.T. Chen, Y.U. Idzerda, H.-J. Lin, N.V. Smith, G. Meigs, E. Chaban, G.H. Ho, E. Pellegrin, and F. Sette, Phys. Rev. Lett. **75**, 152 (1995).
38. U. Fano, Phys. Rev. A **178**, 131 (1969).
39. D. Weller, J. Stöhr, R. Nakajima, A. Carl, M.G. Samant, C. Chappert, R. Mégy, P. Beauvillain, P. Veillet, and G.A. Held, Phys. Rev. Lett. **75**, 3752 (1995).
40. R. Wuand and A.J. Freeman, Phys. Rev. Lett. **73**, 1994 (1994).
41. W. L. O'Brien, B.P. Tonner, G.R. Harp, and S.S.P. Parkin, J. Appl. Phys. **76**, 6462 (1994).
42. D. Rioux, B. Allen, H. Höchst, D. Zhao, and D.L. Huber, Phys. Rev. B **56**, 753 (1997).
43. J. Schwitalla and H. Ebert, Phys. Rev. Lett. **80**, 4586 (1998).
44. J. Vogel and M. Sacchi, Phys. Rev. B **49**, 3230 (1994).
45. X. Le Cann, C. Boeglin, B. Carrière, and K. Hricovini, Phys. Rev. B **54**, 373 (1996).
46. J. Hunter Dunn, D. Arvanitis, and N. Mårtensson, Phys. Rev. B **54**, R11157 (1996).
47. G. Möllenstedt and F. Lenz: Electron emission microscopy. In: L. Marton (ed.), Advances in Electronics and Electron Physics, Academic Press, London (1963).
48. H. Bethke and M. Klaua, Ultramicroscopy **11**, 207 (1983).
49. W. Engel, M.E. Kordesch, H.H. Rotermund, S. Kubala, and A. von Oertzen, Ultramicroscopy **36**, 148 (1991).
50. M.E. Kordesch, W. Engel, G.J. Lapeyre, E. Zeitler, and A.M. Bradshaw, Appl. Phys. A **49**, 399 (1989).
51. M. Mundschau, M.E. Kordesch, B. Rausenberger, W. Engel, A.M. Bradshaw, and E. Zeitler, Surf. Sci. **227**, 246 (1990).
52. H.H. Rotermund, S. Nettesheim, A. von Oertzen, and G. Ertl, Surf. Sci. **275**, L645 (1992).
53. S. Nettesheim, A. von Oertzen, H.H. Rotermund, and G. Ertl, J. Chem. Phys. **98**, 9977 (1993).
54. W. Telieps and E. Bauer, Ultramicroscopy **17**, 57 (1985).
55. B.P. Tonner and G.R. Harp, Rev. Sci. Instrum. **59**, 853 (1988).
56. Ch. Ziethen, O. Schmidt, G.H. Fecher, C.M. Schneider, G. Schönhense, R. Frömter, M. Seider, K. Grzelakowski, M. Merkel, D. Funnemann, W. Swiech, H. Gundlach, and J. Kirschner, J. Electron Spectrosc. Relat. Phenom. **88–91**, 983 (1998).
57. G. De Stasio, L. Perfetti, B. Gilbert, O. Fauchox, M. Capozi, P. Perfetti, G. Margaritondo, and B.P. Tonner, Rev. Sci. Instrum. **70**, 1740 (1999).
58. E. Bauer, Appl. Surf. Sci. **92**, 20 (1996).
59. R. Fink, M.R. Weiss, E. Umbach, D. Preikszas, H. Rose, R. Spehr, P. Hartel, W. Engel, R. Degenhardt, R. Wichtendahl, H. Kuhlenbeck, W. Erlebach, K. Ihmann, R. Schlögl, H.-J. Freund, A.M. Bradshaw, G. Lilienkamp, T. Schmidt, E. Bauer, and G. Benner, J. Electron Spectrosc. Relat. Phenom. **84**, 231 (1997).

60. W. Kuch, J. Gilles, F. Offi, S.S. Kang, S. Imada, S. Suga, and J. Kirschner, Surf. Sci. **480**, 153 (2001).
61. J. Thomassen, F. May, B. Feldmann, M. Wuttig, and H. Ibach, Phys. Rev. Lett. **69**, 3831 (1992).
62. M.T. Kief and W.F. Egelhoff, Jr., Phys. Rev. B **47**, 10785 (1993).
63. K. Heinz, S. Müller, and P. Bayer, Surf. Sci. **337**, 215 (1995).
64. P. Bayer, S. Müller, P. Schmailzl, and K. Heinz, Phys. Rev. B **48**, 17611 (1993).
65. D. Li, M. Freitag, J. Pearson, Z.Q. Qiu, and S.D. Bader, Phys. Rev. Lett. **72**, 3112 (1994).
66. M. Straub, R. Vollmer, and J. Kirschner, Phys. Rev. Lett. **77**, 743 (1996).
67. M. Wuttig, B. Feldmann, J. Thomassen, F. May, H. Zillgen, A. Brodde, H. Hannemann, and H. Neddermayer, Surf. Sci. **291**, 14 (1993).
68. J. Giergiel, J. Kirschner, J. Landgraf, J. Shen, and J. Woltersdorf, Surf. Sci. **310**, 1 (1994).
69. J. Giergiel, J. Shen, J. Woltersdorf, A. Kirilyuk, and J. Kirschner, Phys. Rev. B **52**, 8528 (1995).
70. M.-T. Lin, J. Shen, W. Kuch, H. Jenniches, M. Klaua, C.M. Schneider, and J. Kirschner, Surf. Sci. **410**, 290 (1998).
71. S.S. Kang, W. Kuch, and J. Kirschner, Phys. Rev. B **63**, 024401 (2001).
72. V.L. Moruzzi, P.M. Marcus, K. Schwarz, and P. Mohn, Phys. Rev. B **34**, 1784 (1986).
73. V.L. Moruzzi, P.M. Marcus, and J. Kübler, Phys. Rev. B **39**, 6957 (1989).
74. P.M. Marcus, S.L. Qiu, and V.L. Moruzzi, J. Phys.: Cond. Matt. **11**, 5709 (1999).
75. E.J. Escorcia-Aparicio, R.K. Kawakami, and Z.Q. Qiu, Phys. Rev. B **54**, 4155 (1996).
76. R.K. Kawakami, E.J. Escorcia-Aparicio, Z.Q. Qiu, J. Appl. Phys. **79**, 4532 (1996).
77. W. Kuch and S.S.P. Parkin, Europhys. Lett. **37**, 465 (1997).
78. W. Kuch and S.S.P. Parkin, J. Magn. Magn. Mater. **184**, 127 (1998).
79. W. Kuch, J. Gilles, F. Offi, S.S. Kang, S. Imada, S. Suga, and J. Kirschner, J. Electron Spectrosc. Relat. Phenom. **109**, 249 (2000).
80. D. Schmitz, C. Charton, A. Scholl, C. Carbone, and W. Eberhardt, Phys. Rev. B **59**, 4327 (1999).
81. W. L. O'Brien and B.P. Tonner, Surf. Sci. **334**, 10 (1995).
82. W. L. O'Brien and B.P. Tonner, Phys. Rev. B **52**, 15332 (1995).
83. X. Gao, M. Salvietti, W. Kuch, C.M. Schneider, and J. Kirschner, Phys. Rev. B **58**, 15426 (1998).
84. R. Kläsges, D. Schmitz, C. Carbone, W. Eberhardt, and T. Kachel, Solid State Commun. **107**, 13 (1998).
85. R. Lorenz and J. Hafner, Phys. Rev. B **54**, 15937 (1996).
86. T. Asada and S. Blügel, Phys. Rev. Lett. **79**, 507 (1997).
87. E.G. Moroni, G. Kresse, and J. Hafner, J. Phys.: Cond. Matt. **11**, L35 (1999).
88. D. Spisak and J. Hafner, Phys. Rev. B **62**, 9575 (2000).
89. R. Lorenz and J. Hafner, Phys. Rev. B **58**, 5197 (1998).
90. J.C. Slonczewski, Phys. Rev. Lett. **67**, 3172 (1991).
91. J.C. Slonczewski, J. Magn. Magn. Mater. **150**, 13 (1995).
92. P. Bruno, Phys. Rev. B **39**, 865 (1989).
93. W. Kuch, J. Gilles, S.S. Kang, S. Imada, S. Suga, and J. Kirschner, Phys. Rev. B **62**, 3824 (2000).
94. P. Krams, F. Lauks, R.L. Stamps, B. Hillebrands, and G. Güntherodt, Phys. Rev. Lett. **69**, 3674 (1992).
95. M. Kowalewski, C.M. Schneider, and B. Heinrich, Phys. Rev. B **47**, 8748 (1993).
96. F. Huang, M.T. Kief, G.J. Mankey, and R.F. Willis, Phys. Rev. B **49**, 3962 (1994).
97. W. L. O'Brien and B.P. Tonner, Phys. Rev. B **49**, 15370 (1994).

98. B. Schulz and K. Baberschke, Phys. Rev. B **50**, 13467 (1994).
99. M. Farle, B. Mirwald-Schulz, A.N. Anisimov, W. Platow, and K. Baberschke, Phys. Rev. B **55**, 3708 (1997).
100. Y. Yafet and E.M. Gyorgy, Phys. Rev. B **38**, 9145 (1988).
101. M. Speckmann, H.P. Oepen, and H. Ibach, Phys. Rev. Lett. **75**, 2035 (1995).
102. F. Wilhelm, P. Poulopoulos, P. Srivastava, H. Wende, M. Farle, K. Baberschke, M. Angelakeris, N.K. Flevaris, W. Grange, J.-P. Kappler, G. Ghiringhelli, and N.B. Brookes, Phys. Rev. B **61**, 8647 (2000).
103. M.R. Weiss, R. Follath, K.J.S. Sawhney, F. Senf, J. Bahrdt, W. Frentrup, A. Gaupp, S. Sasaki, M. Scheer, H.-C. Mertins, D. Abramsohn, F. Schäfers, W. Kuch, and W. Mahler, Nucl. Instr. and Meth. A, **467–468**, 449 (2001).
104. D.W. Turner, I.R. Plummer, and H.Q. Porter, Rev. Sci. Instrum. **59**, 45 (1988).
105. G.K.L. Marx, V. Gerheim, and G. Schönhense, J. Electron Spectrosc. Relat. Phenom. **84**, 251 (1997).
106. Y. Sakai, M. Kato, S. Masuda, Y. Harada, and T. Ichinokawa, Surf. Rev. Lett. **5**, 1199 (1998).
107. T. Schmidt, S. Heun, J. Slezak, J. Diaz, K.C. Prince, G. Lilienkamp, and E. Bauer, Surf. Rev. Lett. **5**, 1287 (1998).
108. G. Rossi, G. Panaccione, F. Sirotti, and N.A. Cherepkov, Phys. Rev. B **55**, 11483 (1997).
109. C.S. Fadley: Recent developments in photoelectron diffraction. In: J. Kanamori and A. Kotani (ed.), Core-Level Spectroscopy in Condensed Systems, Springer, Berlin (1988).
110. C.S. Fadley, Surf. Sci. Rep. **19**, 231 (1993).
111. H. Daimon, T. Nakatani, S. Imada, S. Suga, Y. Kagoshima, and T. Miyahara, Rev. Sci. Instrum. **66**, 1510 (1995).
112. M. Bonfim, G. Ghiringhelli, F. Montaigne, S. Pizzini, N.B. Brookes, F. Petroff, J. Vogel, J. Camarero, and A. Fontaine, Phys. Rev. Lett. **86**, 3646 (2001).